Picocavity-Enhanced Raman Spectroscopy of Physisorbed H_2 and D_2 Molecules

Akitoshi Shiotari,[1,*] Shuyi Liu,[1,†] George Trenins,[2] Toshiki Sugimoto,[3,4] Martin Wolf,[1] Mariana Rossi,[2,‡] and Takashi Kumagai[3,4,§]

[1]*Department of Physical Chemistry, Fritz-Haber Institute of the Max-Planck Society, Faradayweg 4-6, 14195 Berlin, Germany*
[2]*Max-Planck-Institute for Structure and Dynamics of Matter, 22761 Hamburg, Germany*
[3]*Institute for Molecular Science, National Institutes of Natural Sciences, 444-8585 Okazaki, Japan*
[4]*The Graduate University for Advanced Studies, SOKENDAI, 240-0193 Hayama, Japan*

(Received 4 June 2024; revised 12 February 2025; accepted 28 April 2025; published 20 May 2025)

We report on tip-enhanced Raman spectroscopy of H_2 and D_2 molecules physisorbed within a plasmonic picocavity at 10 K. The intense Raman peaks resulting from the rotational and vibrational transitions are observed at subnanometer gap distances of the junction formed by an Ag tip and an Ag(111) surface, where a picocavity-enhanced field plays a crucial role. A significant redshift of the H-H stretch frequency is observed as the gap distance decreases, while the D-D stretch frequency is unaffected. Density functional theory, path-integral molecular dynamics, and quantum anharmonic vibrational energy calculations suggest that this unexpected isotope effect is explained by a different molecular density between H_2 and D_2 on the surface.

DOI: 10.1103/PhysRevLett.134.206901

The adsorption of hydrogen molecules on solid surfaces is the first step in permeation for fuel storage [1], catalytic hydrogenation [2], hydrogen embrittlement [3], and nuclear-spin isomer conversion [4]. To understand and control the elementary processes in such physical and chemical phenomena, hydrogen adsorption has been intensively studied in surface science [5–7]. Specifically, hydrogen, the lightest molecule, exhibits unique quantum effects that differ from those of other molecules when it is physisorbed on a surface through van der Waals interactions [8–17]. However, only a few methods are available for characterizing such physisorption systems as the weak adsorption energy (< 100 meV) necessitates measurements at cryogenic temperatures. Low-temperature scanning tunneling microscopy has been employed as a local characterization technique to investigate the dynamics of hydrogen molecules weakly adsorbed on surfaces [18–28]. Several studies have observed characteristic features in conductance spectra, attributed to the rotational transition of molecular hydrogen in the scanning tunneling microscopy (STM) junction [21–24]. However, the interpretation remains controversial; the features within the corresponding energy range [30–60 meV ($\sim$240–480 cm^{-1}) for H_2] could be attributed to configuration switching [18,29,30], to a molecule-substrate stretching mode [31], or to multiple phonon excitation [32]. Additionally, the stretching mode has never been observed in these studies.

Raman spectroscopy is a promising technique for characterizing hydrogen molecules on surfaces, as it allows the observation of both rotational and vibrational transitions of homonuclear diatomic molecules. Although the detection demands exceptional sensitivity due to the intrinsically small cross section, single-molecule detection can be achieved by tip-enhanced Raman spectroscopy (TERS) and surface-enhanced Raman spectroscopy (SERS) [33–37]. Recent studies have established that picocavities, atomic-scale protrusions present in plasmonic nanojunctions, play a crucial role in achieving extreme confinement of the electromagnetic field to angstrom scales [37–39], resulting in a significant enhancement of Raman scattering [40–42] and ultrahigh spatial resolution [43–46]. Yet, the exceptional sensitivity in TERS and SERS has been demonstrated primarily for organic molecules chemisorbed onto the substrate, where the enhancement benefits from chemical effects arising from the molecule-surface (and molecule-tip) interactions [47]. Therefore, applying TERS or SERS to physisorbed systems has remained challenging.

Here, we demonstrate that low-temperature TERS (LT-TERS) can detect hydrogen molecules physisorbed onto an Ag(111) surface with an Ag tip [Fig. 1(a), inset], allowing for the identification of their rotational and vibrational states. Furthermore, precise gap-distance control enables us to investigate not only the contribution of the

*Contact author: shiotari@fhi-berlin.mpg.de
†Present address: Huazhong University of Science and Technology, Wuhan, China.
‡Contact author: mariana.rossi@mpsd.mpg.de
§Contact author: kuma@ims.ac.jp

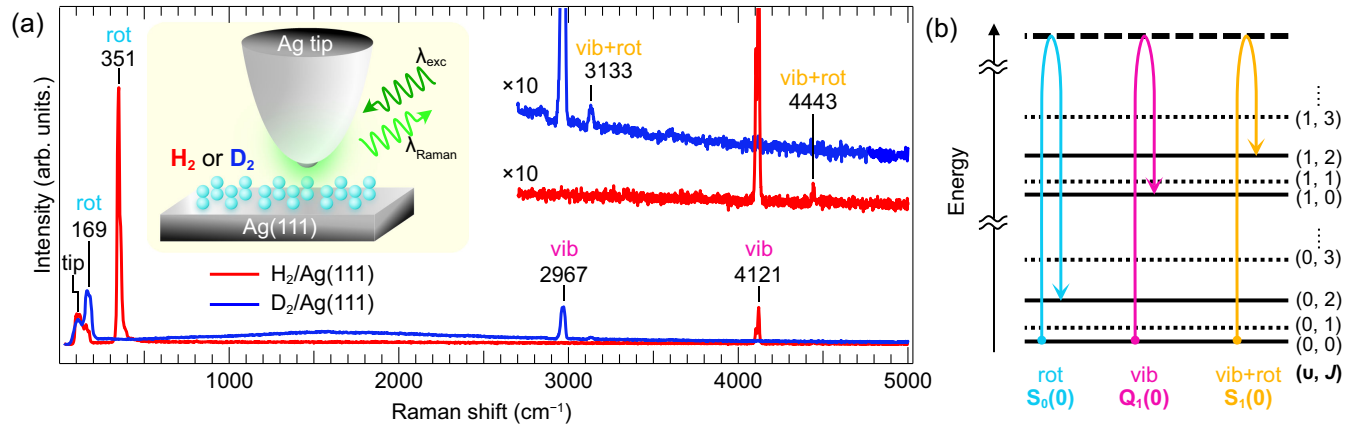

FIG. 1. (a) TERS spectra of H_2 (red) and D_2 (blue) on Ag(111) with a Ag tip at 10 K (sample bias voltage $V_s = 10$ mV, tunneling current $I_t = 1.0$ nA). The left inset shows a schematic of the experiment. λ_{exc} and λ_{Raman} denote the wavelength of the incident laser and Raman scattering, respectively. The right inset shows magnified spectra in the high wave number regions. The peak originating from tip phonon modes is denoted as "tip." (b) Energy diagram of the vibrational and rotational levels of an H_2 or D_2 molecule. The solid lines represent the levels for *para*-H_2 and *ortho*-D_2, while the dotted lines are those for *ortho*-H_2 and *para*-D_2. The dashed bold line represents a virtual state. The arrows indicate Raman-active transitions referred to as "rot," "vib," and "rot + vib." υ and J denote the vibrational and rotational quantum numbers, respectively.

picocavity field to the Raman scattering process but also the influence of tip proximity on the rotational and vibrational energies of the molecules through nontrivial nuclear quantum effects. Density functional theory (DFT), path-integral molecular dynamics, and quantum vibrational energy calculations suggest that the tip-molecule-surface potential energy profiles are critically affected by the intermolecular and tip-molecular interactions, leading to unusual isotope effects on vibrational frequencies.

The LT-TERS experiments were performed in an ultra-high vacuum chamber [see Sec. I-A of Supplemental Material (SM) [48]]. The 532-nm incident laser beam was linearly polarized along the tip axis and focused on the apex of a focused-ion-beam-sharpened Ag tip [40,42] using an *in situ* parabolic mirror, and the scattering light was detected by an *ex situ* spectrometer. We conducted DFT calculations [50,51] of H_2/D_2 on a 4×4 Ag(111) (periodic) surface, employing the Perdew-Burke-Ernzerhof exchange-correlation functional and screened pairwise van der Waals interactions [52] (see SM Sec. I-B [48]). The preferred adsorption sites (fcc or hcp hollow) and binding energies (~30 meV) were in very good agreement with previous studies of isolated molecules on the surface [55,65]. Unless specified otherwise, we considered a coverage of 0.69 monolayer (ML), motivated by the results of path-integral molecular dynamics simulations at low temperature (see SM Sec. I-B [48]). At 0.69 ML coverage, the intermolecular attractive interaction increases the binding energy by 55 meV compared to the lowest coverage of 0.06 ML considered here (Fig. S3). Over the sample, we placed the Ag-tip model shown in SM Sec. I-B [48] (see also Fig. S4), which was also previously discussed in Refs. [41,46,54].

H_2 or D_2 gas was introduced into the chamber where a clean Ag(111) surface was cooled at 10 K (see SM Sec. I-A [48]). Regardless of laser illumination, no static hydrogen molecules on the surface were imaged with STM (Fig. S1). In contrast, clear peaks were observed in TERS spectra under these conditions. Figure 1(a) displays typical TERS spectra of H_2 and D_2 on Ag(111). For H_2, intense peaks were observed at 351 and 4121 cm^{-1}, along with a weak peak at 4443 cm^{-1}. Similarly, for D_2, intense peaks appeared at 169 and 2967 cm^{-1}, with a weak peak at 3133 cm^{-1}. The three peaks can be assigned to rotational and vibrational modes of hydrogen. Note that broad or asymmetric peak shapes are artifacts in the wide wave number range spectra (see SM Sec. I-A [48]). The feature around 100 cm^{-1} common to both spectra originates from phonon modes of the Ag tip [41,66], which is present even in the absence of hydrogen adsorption (Fig. S2). Figure 1(b) depicts the energy diagram of rotational and vibrational levels and allowed transitions under the Raman selection rule. The observed peaks, in order from lowest to highest, correspond to the lowest-energy rotational transition [$S_0(0)$; "rot" labeled in Fig. 1(a)], the lowest-energy vibrational transition [$Q_1(0)$; "vib"], and their combination [$S_1(0)$; "rot + vib"], respectively. The three modes were also observed in high-resolution electron energy loss spectroscopy of hydrogen on a polycrystalline Ag film [8] and a Cu(001) surface [9] at approximately 10–12 K; however, better energy resolution (< 10 cm^{-1}) in TERS than that of the electron energy loss spectroscopy (> 28 cm^{-1} [9]) makes the redshifts from gas-phase hydrogen more discernible (Table S4). We should also note that only the stable nuclear-spin isomer of each isotope, i.e., *para*-H_2 and *ortho*-D_2 [Fig. 1(b)], is detected in TERS

(Fig. S2). On the surface, the stable isomer is dominant due to the *ortho-para* conversion [4,8,55] (see SM Sec. II-A [48]).

The rotational transition at 351 cm^{-1} for $H_2/Ag(111)$ [Fig. 1(a)] is slightly redshifted from 354 cm^{-1} in the gas phase [62]. We calculate the H-H bond length to be 75.4 pm on Ag(111) (cf. 75.1 pm in the gas phase). Considering a rigid-rotor approximation, the rotational transition energy of *para*-H_2 is calculated to be 353 cm^{-1} on the surface, compared to 356 cm^{-1} in the gas phase, showing good agreement with the experiment. Notably, the H-H bond length of H_2 on Ag(111) varied by only 0.06 pm at the closest tip position with respect to simulations without any tip. This suggests that the hydrogen molecules on the surface and in the STM junction behave as nearly free rotors.

In the TERS spectrum [Fig. 1(a)], the vibrational frequency of 4121 cm^{-1} exhibits a redshift relative to the gas-phase value of 4161 cm^{-1} [62]. The vibrational transition energy is calculated to be 4088 cm^{-1} on the surface (without the Ag tip), after applying a scale factor to the calculations performed in the harmonic approximation (see SM Sec. I-C [48]; see also Fig. S8 for a simulated LT-TERS spectrum [46]). The slight discrepancy between the experimental and calculated frequencies is consistent with the typical spurious softening of the Perdew-Burke-Ernzerhof functional. Compared to the calculated gas-phase value, the vibrational frequency shows a redshift of ~73 cm^{-1} upon the adsorption, which is larger than, but in reasonable agreement with the experiment.

The TERS intensity is strongly correlated with the localized surface plasmonic resonance (LSPR) of the tip-sample junction. In general, two types of enhancement mechanisms contribute to TERS [36,47]: electromagnetic enhancement through LSPR and chemical enhancement originating from charge transfer between the target molecule and the tip or surface. In physisorption systems, the electromagnetic enhancement is expected to be dominant.

To elucidate the role of electromagnetic enhancement, it is crucial to investigate the gap-distance dependence of TERS signals. Figure 2(a) shows the waterfall plot of the gap-distance-dependent TERS spectra recorded for $D_2/Ag(111)$. When the tip approaches the surface, the TERS intensities of the rotational and vibrational modes increase apparently exponentially [Fig. 2(b)], in agreement with the previously reported analytical model simplifying a plasmonic tip as a point dipole [60]. A broad background with a maximum at ~590 nm is attributed to electronic Raman scattering, which reflects the spectral response of the LSPR in the junction [67]. The gap-distance-dependent intensities of both rotational and vibrational modes closely follow the plasmonic feature [Fig. 2(b)], indicating the dominant contribution of the gap-mode plasmon to the TERS enhancement. Additionally, we observed that changes in both the plasmon background and the molecular

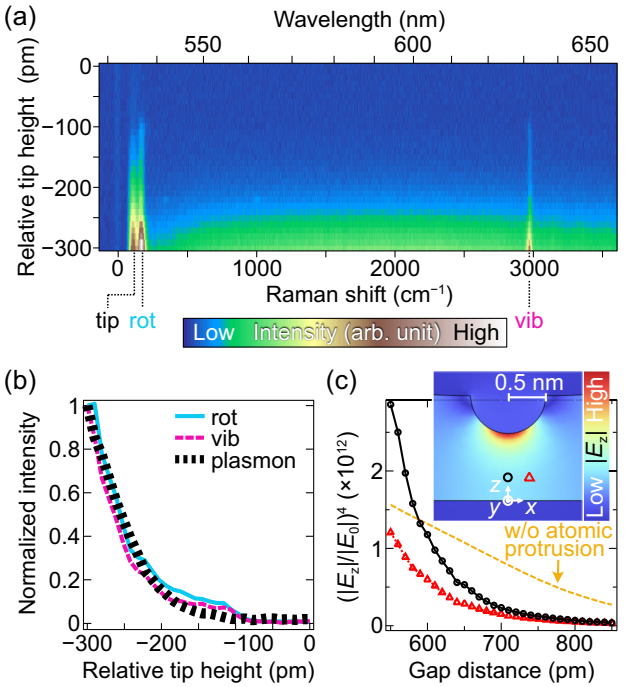

FIG. 2. (a) Waterfall plot for the TERS spectra during the tip approach to $D_2/Ag(111)$. The origin of the vertical axis corresponds to a tip height 100 pm above the STM set point ($V_s = 10$ mV, $I_t = 0.1$ nA). (b) Tip-height dependence of the Raman intensities, corresponding to the vertical line profiles of "rot," "vib," and the plasmonic background (2000 cm^{-1}). The intensity is normalized for each profile. (c) Gap-distance dependence of the field enhancement factor simulated by the finite element method. The STM junction with a plasmonic picocavity is modeled using an Ag tip (30-nm radius of curvature) with an atomic-scale protrusion (0.5-nm radius) and a flat Ag sample plate (Fig. S9). The vertical electric field E_z at $\lambda_{exc} = 532$ nm is sampled and normalized with the incident field E_0. The inset shows the $|E_z|$ distribution at a tip-sample gap distance of 0.9 nm. The black curve represents the field enhancement factor $(|E_z|/|E_0|)^4$ sampling at the location of the D_2 just below the tip (circle marker in the inset), while the red curve is that at the nearest neighboring D_2 (triangle). The orange curve shows the field enhancement at the same sampling point as the black curve but using an Ag tip without the atomic-scale protrusion.

Raman peak occurred by an accidental modification of the tip-apex structure (Fig. S11), implying that the TERS enhancement is susceptible to the atomic-scale structure of the tip apex, which generates a plasmonic picocavity.

The gap-distance dependence of the TERS intensities is well reproduced by simulating the electronic field distribution in the Ag-tip–Ag-surface junction using the finite element method (see SM Sec. I-E [48]). To model the plasmonic picocavity, we assume an atomic-scale protrusion (0.5-nm radius of curvature) attached to a blunt tip body (Fig. S9). The black curve in Fig. 2(c) shows the field enhancement at the expected position of a D_2 molecule located beneath the Ag tip, indicating a steep increase as the tip approaches. We confirmed the critical role of this

subnanometric structure in TERS; as shown by the orange curve in Fig. 2(c), the tip without the atomic-scale protrusion exhibits a more moderate increase of the field enhancement as the tip approaches, which does not reproduce the experimental data [Fig. 2(b)]. The red curve in Fig. 2(c) shows the field enhancement at a possible position of the nearest neighboring molecule [Fig. 2(c), inset], indicating much lower enhancement. Therefore, TERS can achieve "nearly" single-molecule sensitivity, even for physisorption systems. The contribution of LSPR to the TERS intensity was further confirmed by our excitation-wavelength dependent measurements (SM Sec. II-B [48]); a strong TERS peak was observed only when the scattering light wavelength matches with the resonance range of the LSPR (Fig. S10).

TERS reveals the sensitivity of the rotational and vibrational states to the interactions between a target molecule and its local environment. Figures 3(a)–3(d) show the gap-distance dependence of high-resolution TERS spectra focusing on the rotational and vibrational modes of H_2 and D_2. Notably, only the vibrational frequency of H_2 exhibits a significant redshift as the gap distance decreases [Fig. 3(c)]; H_2 shows a peak shift $\Delta\nu$ of -33 cm^{-1} with a 200 pm displacement of the tip, whereas $\Delta\nu$ is merely -2 cm^{-1} for D_2. Additionally, the peak width of the H_2 vibrational mode also increases as the gap distance decreases (see SM Sec. II-C [48] for details). In contrast, the peak positions of the rotational modes for both H_2 [Fig. 3(a)] and D_2 [Fig. 3(b)] are almost unchanged, consistent with our calculations showing that the interatomic distance is independent of the tip height, as described above.

The isotope dependence of the redshift of the vibrational band far exceeds the scale of typical isotope effects. To understand this anomalous behavior, we calculated the potential energy profile $V(d_{\text{mol-surf}}, d_{\text{tip-surf}})$ along the rigid vertical displacement of the center of mass of one molecule between the surface and the tip apex $d_{\text{mol-surf}}$ [Fig. 4(a)], while varying the tip-sample distance $d_{\text{tip-surf}}$ [see profiles (i)–(iv) at different $d_{\text{tip-surf}}$ in Fig. 4(b)]. At each $d_{\text{mol-surf}}$ position, we calculated the H_2 and D_2 harmonic intramolecular vibrational frequency ν_{harm} (see SM Sec. I-C [48]). The calculations indicate a pronounced coupling of the stretch coordinate r_{stretch} with the molecular translation along $d_{\text{mol-surf}}$, evidenced by a steep variation of ν_{harm} along this coordinate (Fig. S7). Furthermore, this variation changes depending on the tip-sample distance, leading us to define $\nu_{\text{harm}}(d_{\text{mol-surf}}, d_{\text{tip-surf}})$. As detailed in SM Sec. I-C [48], for each $d_{\text{tip-surf}}$, we constructed a model 2D Schrödinger equation in the coupled coordinates $d_{\text{mol-surf}}$ and r_{stretch}, parametrized by $V(d_{\text{mol-surf}}, d_{\text{tip-surf}})$ and $\nu_{\text{harm}}(d_{\text{mol-surf}}, d_{\text{tip-surf}})$. The solution of this model gives us the expected intramolecular stretch vibrational transition energy ν for each isotope, fully accounting for the anharmonic coupling between these coordinates. We concluded

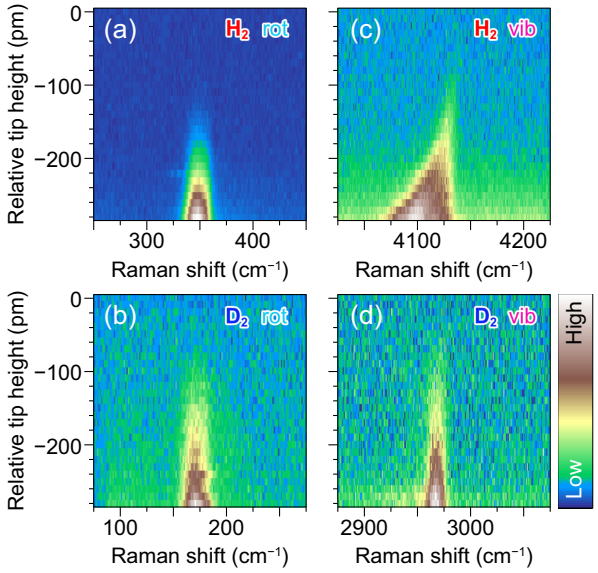

FIG. 3. (a)–(d) Waterfall plots of the high-resolution TERS spectra with different tip heights: (a) H_2 rot, (b) H_2 vib, (c) D_2 rot, and (d) D_2 vib. The origin of the tip height corresponds to a tip height 30 and 70 pm higher than the set point ($V_s = 10$ mV, $I_t = 0.1$ nA) for H_2 and D_2, respectively.

that if both H_2 and D_2 probe the same potential energy profile $V(d_{\text{mol-surf}}, d_{\text{tip-surf}})$ [Fig. 4(b)], for reasonable position-dependent stretch frequencies $\nu_{\text{harm}}(d_{\text{mol-surf}}, d_{\text{tip-surf}})$ the calculated peak shifts $\Delta\nu$ are in a ratio of at most 2:1 for H_2:D_2 (Tables S2 and S3), in disagreement with the measured 16:1 ratio (Fig. 3).

We demonstrate that this discrepancy can be resolved by accounting for density differences between H_2 and D_2. At lower temperatures, the solids formed by H_2 and D_2 have different molar volumes due to nuclear quantum effects [zero-point energy (ZPE) swelling [68]; see also SM Sec. I-B [48]]. As a result, solid D_2 is more than twice as dense as solid H_2 at 4.2 K [69]. Because the interaction potential between the molecules and the surface exhibits almost no corrugation [55], we expect that H_2 adsorbs on Ag(111) at 10 K more sparsely than D_2. To explore a limiting low-density regime, we repeated the calculations discussed in the previous paragraph for a coverage of 0.06 ML of H_2 [Fig. 4(c)]. As shown in Fig. 4(d), the reduced intermolecular interactions at the surface cause the minimum of $V(d_{\text{mol-surf}}, d_{\text{tip-surf}})$ along $d_{\text{mol-surf}}$ to lie closer to the tip instead of closer to the surface, as $d_{\text{tip-surf}}$ decreases [(i) to (iv)]. Consequently, the average position of the molecule center of mass [bullet points in Figs. 4(b) and 4(d)] also shifts toward the tip as $d_{\text{tip-surf}}$ decreases [dotted line in Fig. 4(d)]. Computing ν in this scenario with the 2D quantum model of $d_{\text{mol-surf}}$ and r_{stretch}, we find a larger variation with $d_{\text{tip-surf}}$ than in the higher-density case (Table S2). As shown in Fig. 4(e), considering the higher-density scenario for D_2 (the filled bullets) and the lower-density scenario for H_2 (the empty bullets) can account for

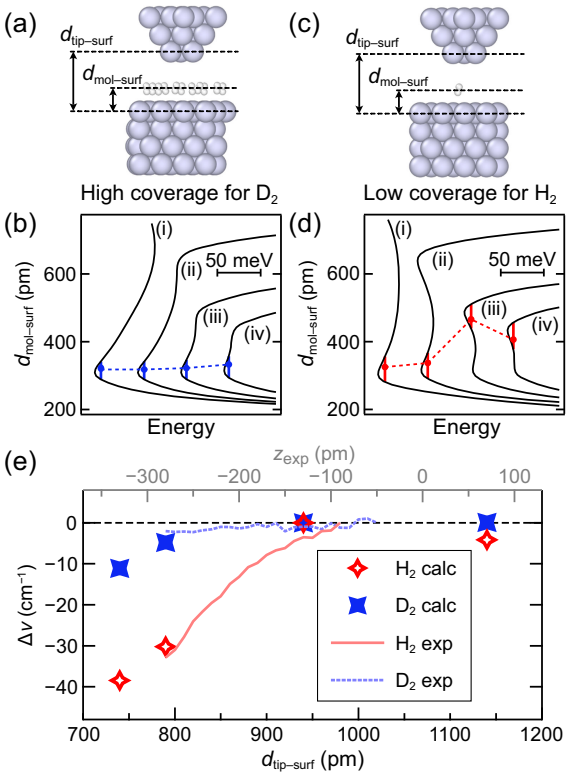

FIG. 4. (a) Simulated atomic structure of the junction at a tip-surface distance $d_{tip\text{-}surf}$ of 0.79 nm at a high coverage (0.69 ML). The light blue and white spheres represent Ag and H atoms, respectively. (b) Energy profiles along $d_{mol\text{-}surf}$ at the high coverage shown in (a). Curves (i)–(iv) indicate profiles obtained at $d_{tip\text{-}surf} = 1.14$, 0.94, 0.79, and 0.74 nm, respectively. For clarity, curves (ii)–(iv) are offset by 50, 100, and 150 meV, respectively, relative to (i) in the horizontal axis. The bullet on each potential indicates the average D_2 position, considering ZPE contributions (Table S3). The vertical lines indicates the ZPE levels and the dashed lines connecting the bullets serve only as a guide to the eye. (c) Same as (a) but at a lower coverage (0.06 ML). (d) Same as (b), but at the lower coverage shown in (c). The bullet on each potential indicates the average H_2 position, considering ZPE contributions (Table S2). (e) Shifts of the intramolecular stretch frequencies $\Delta\nu$ as a function of $d_{tip\text{-}surf}$. The empty red and filled blue bullets represent the calculated values of low-coverage H_2 and high-coverage D_2, respectively. The frequencies at $d_{tip\text{-}surf} = 0.94$ nm are used for the origin of the shifts. The solid red and dashed blue lines represent the experimental $\Delta\nu$ values for H_2 vib [Fig. 3(c)] and D_2 vib [(d)], respectively, as a function of the relative tip height z_{exp} (see SM Sec. II-C [48] for details). The minimum tip height, $z_{exp} = -280$ pm, is aligned with $d_{tip\text{-}surf} = 0.74$ nm.

the large isotope effect in the redshift of the stretch transition as the tip approaches. Figure 4(e) also shows the experimental $\Delta\nu$ values from the plots in Fig. 3 (the solid and dotted curves for H_2 and D_2, respectively; see also Fig. S12). Although the exact gap distance in STM experiment is hard to determine (see SM Sec. II-C [48]), the overlap of the experimental curves with the calculated plots in Fig. 4(e) shows good agreement. The remaining numerical discrepancies can be attributed to the limitation of the DFT level of theory (see SM Sec. I-B [48]), the exact tip-apex geometry, and to the uncertainty in determining the exact local surface coverage. Nevertheless, our results highlight the crucial role of intermolecular interactions in accurately interpreting vibrational spectroscopy of hydrogen isotopes in nanojunctions, where nuclear quantum effects have a significant impact [13].

In summary, with LT-TERS, we observed the rotational and vibrational transitions of local H_2 and D_2 molecules through the interaction with the picocavity field. Our results demonstrate that LT-TERS is applicable to weakly adsorbed molecules, offering deeper insights into the local structures, reactions, and dynamics of adsorbates, such as chemical reactivity at active sites [70] and surface diffusion (spillover) in catalytic processes [71], at the single-molecule level.

Acknowledgments—We thank Adnan Hammud for the Ag-tip fabrication. We thank Jun Yoshinobu and Heiko Appel for helpful discussions. T. S. acknowledges the support of JST FOREST Grant No. JPMJFR221U. T. K. acknowledges the support of JST FOREST Grant No. JPMJFR201J.

Data availability—The data that support the findings of this article are openly available [72].

[1] N. W. Ockwig and T. M. Nenoff, Membranes for hydrogen separation, Chem. Rev. **107**, 4078 (2007).
[2] L. Zhang, M. Zhou, A. Wang, and T. Zhang, Selective hydrogenation over supported metal catalysts: From nanoparticles to single atoms, Chem. Rev. **120**, 683 (2019).
[3] X. Li, X. Ma, J. Zhang, E. Akiyama, Y. Wang, and X. Song, Review of hydrogen embrittlement in metals: Hydrogen diffusion, hydrogen characterization, hydrogen embrittlement mechanism and prevention, Acta Metall. Sin. **33**, 759 (2020).
[4] K. Fukutani and T. Sugimoto, Physisorption and ortho–para conversion of molecular hydrogen on solid surfaces, Prog. Surf. Sci. **88**, 279 (2013).
[5] K. Christmann, Interaction of hydrogen with solid surfaces, Surf. Sci. Rep. **9**, 1 (1988).
[6] G. Vidali, G. Ihm, H.-Y. Kim, and M. W. Cole, Potentials of physical adsorption, Surf. Sci. Rep. **12**, 135 (1991).
[7] L. W. Bruch, R. D. Diehl, and J. A. Venables, Progress in the measurement and modeling of physisorbed layers, Rev. Mod. Phys. **79**, 1381 (2007).
[8] P. Avouris, D. Schmeisser, and J. E. Demuth, Observation of rotational excitations of H_2 adsorbed on Ag surfaces, Phys. Rev. Lett. **48**, 199 (1982).
[9] S. Andersson and J. Harris, Observation of rotational transitions for H_2, D_2, and HD adsorbed on Cu(100), Phys. Rev. Lett. **48**, 545 (1982).
[10] C. F. Yu, K. B. Whaley, C. S. Hogg, and S. J. Sibener, Selective adsorption resonances in the scattering of n-H_2, p-H_2, n-D_2 and o-D_2 from Ag(111), Phys. Rev. Lett. **51**, 2210 (1983).

[11] M. Sakurai, T. Okano, and Y. Tuzi, Ortho-para conversion of n-H_2 physisorbed on Ag(111) near two-dimensional condensation conditions, Appl. Surf. Sci. **33**, 245 (1988).
[12] G. Anger, A. Winkler, and K. Rendulic, Adsorption and desorption kinetics in the systems H_2/Cu(111), H_2/Cu(110) and H_2/Cu(100), Surf. Sci. **220**, 1 (1989).
[13] K. A. Williams, B. K. Pradhan, P. C. Eklund, M. K. Kostov, and M. W. Cole, Raman spectroscopic investigation of H_2, HD, and D_2 physisorption on ropes of single-walled, carbon nanotubes, Phys. Rev. Lett. **88**, 165502 (2002).
[14] K. Fukutani, K. Yoshida, M. Wilde, W. A. Diño, M. Matsumoto, and T. Okano, Photostimulated desorption and ortho-para conversion of H_2 on Ag surfaces, Phys. Rev. Lett. **90**, 096103 (2003).
[15] K. Niki, T. Kawauchi, M. Matsumoto, K. Fukutani, and T. Okano, Mechanism of the ortho-para conversion of hydrogen on Ag surfaces, Phys. Rev. B **77**, 201404(R) (2008).
[16] T. Sugimoto and K. Fukutani, Effects of rotational-symmetry breaking on physisorption of ortho-and para-H_2 on Ag(111), Phys. Rev. Lett. **112**, 146101 (2014).
[17] T. Sugimoto, Y. Kunisada, and K. Fukutani, Inelastic electron tunneling mediated by a molecular quantum rotator, Phys. Rev. B **96**, 241409(R) (2017).
[18] J. A. Gupta, C. P. Lutz, A. J. Heinrich, and D. M. Eigler, Strongly coverage-dependent excitations of adsorbed molecular hydrogen, Phys. Rev. B **71**, 115416 (2005).
[19] R. Temirov, S. Soubatch, O. Neucheva, A. C. Lassise, and F. S. Tautz, A novel method achieving ultra-high geometrical resolution in scanning tunnelling microscopy, New J. Phys. **10**, 053012 (2008).
[20] C. Lotze, M. Corso, K. J. Franke, F. von Oppen, and J. I. Pascual, Driving a macroscopic oscillator with the stochastic motion of a hydrogen molecule, Science **338**, 779 (2012).
[21] S. Li, A. Yu, F. Toledo, Z. Han, H. Wang, H. Y. He, R. Wu, and W. Ho, Rotational and vibrational excitations of a hydrogen molecule trapped within a nanocavity of tunable dimension, Phys. Rev. Lett. **111**, 146102 (2013).
[22] F. D. Natterer, F. Patthey, and H. Brune, Distinction of nuclear spin states with the scanning tunneling microscope, Phys. Rev. Lett. **111**, 175303 (2013).
[23] F. D. Natterer, F. Patthey, and H. Brune, Resonant-enhanced spectroscopy of molecular rotations with a scanning tunneling microscope, ACS Nano **8**, 7099 (2014).
[24] A. J. Therrien, A. Pronschinske, C. J. Murphy, E. A. Lewis, M. L. Liriano, M. D. Marcinkowski, and E. C. H. Sykes, Collective effects in physisorbed molecular hydrogen on Ni/Au(111), Phys. Rev. B **92**, 161407(R) (2015).
[25] S. Liu, A. Shiotari, D. Baugh, M. Wolf, and T. Kumagai, Enhanced resolution imaging of ultrathin ZnO layers on Ag(111) by multiple hydrogen molecules in a scanning tunneling microscope junction, Phys. Rev. B **97**, 195417 (2018).
[26] P. Merino, A. Rosławska, C. C. Leon, A. Grewal, C. Große, C. González, K. Kuhnke, and K. Kern, A single hydrogen molecule as an intensity chopper in an electrically driven plasmonic nanocavity, Nano Lett. **19**, 235 (2018).
[27] L. Wang, Y. Xia, and W. Ho, Atomic-scale quantum sensing based on the ultrafast coherence of an H_2 molecule in an STM cavity, Science **376**, 401 (2022).
[28] L. Wang, D. Bai, Y. Xia, and W. Ho, Electrical manipulation of quantum coherence in a two-level molecular system, Phys. Rev. Lett. **130**, 096201 (2023).
[29] W. H. A. Thijssen, D. Djukic, A. F. Otte, R. H. Bremmer, and J. M. van Ruitenbeek, Vibrationally induced two-level systems in single-molecule junctions, Phys. Rev. Lett. **97**, 226806 (2006).
[30] A. Halbritter, P. Makk, S. Csonka, and G. Mihály, Huge negative differential conductance in $Au-H_2$ molecular nanojunctions, Phys. Rev. B **77**, 075402 (2008).
[31] Y. Li, S. Kaneko, S. Fujii, and M. Kiguchi, Symmetry of single hydrogen molecular junction with Au, Ag, and Cu electrodes, J. Phys. Chem. C **119**, 19143 (2015).
[32] M. L. Trouwborst, E. H. Huisman, S. J. van der Molen, and B. J. van Wees, Bistable hysteresis and resistance switching in hydrogen-gold junctions, Phys. Rev. B **80**, 081407(R) (2009).
[33] G. Haran, Single-molecule Raman spectroscopy: A probe of surface dynamics and plasmonic fields, Acc. Chem. Res. **43**, 1135 (2010).
[34] S.-Y. Ding, J. Yi, J.-F. Li, B. Ren, D.-Y. Wu, R. Panneerselvam, and Z.-Q. Tian, Nanostructure-based plasmon-enhanced Raman spectroscopy for surface analysis of materials, Nat. Rev. Mater. **1**, 16021 (2016).
[35] X. Wang, S.-C. Huang, S. Hu, S. Yan, and B. Ren, Fundamental understanding and applications of plasmon-enhanced Raman spectroscopy, Nat. Rev. Phys. **2**, 253 (2020).
[36] T. I. Itoh, M. Procházka, Z.-C. Dong, W. Ji, Y. S. Yamamoto, Y. Zhang, and Y. Ozaki, Toward a new era of SERS and TERS at the nanometer scale: From fundamentals to innovative applications, Chem. Rev. **123**, 1552 (2023).
[37] C. Höppener, J. Aizpurua, H. Chen, S. Gräfe, A. Jorio, S. Kupfer, Z. Zhang, and V. Deckert, Tip-enhanced Raman scattering, Nat. Rev. Methods Primers **4**, 47 (2024).
[38] F. Benz, M. K. Schmidt, A. Dreismann, R. Chikkaraddy, Y. Zhang, A. Demetriadou, C. Carnegie, H. Ohadi, B. De Nijs, R. Esteban, J. Aizpurua, and J. J. Baumberg, Single-molecule optomechanics in "picocavities", Science **354**, 726 (2016).
[39] M. Urbieta, M. Barbry, Y. Zhang, P. Koval, D. Sánchez-Portal, N. Zabala, and J. Aizpurua, Atomic-scale lightning rod effect in plasmonic picocavities: A classical view to a quantum effect, ACS Nano **12**, 585 (2018).
[40] S. Liu, M. Müller, Y. Sun, I. Hamada, A. Hammud, M. Wolf, and T. Kumagai, Resolving the correlation between tip-enhanced resonance raman scattering and local electronic states with 1 nm resolution, Nano Lett. **19**, 5725 (2019).
[41] S. Liu, F. P. Bonafe, H. Appel, A. Rubio, M. Wolf, and T. Kumagai, Inelastic light scattering in the vicinity of a single-atom quantum point contact in a plasmonic picocavity, ACS Nano **17**, 10172 (2023).
[42] Y. Park, I. Hamada, A. Hammud, T. Kumagai, M. Wolf, and A. Shiotari, Atomic-precision control of plasmon-induced single-molecule switching in a metal–semiconductor nanojunction, Nat. Commun. **15**, 6709 (2024).
[43] R. Zhang, Y. Zhang, Z. Dong, S. Jiang, C. Zhang, L. Chen, L. Zhang, Y. Liao, J. Aizpurua, Y. Luo, J. L. Yang, and J. G. Hou, Chemical mapping of a single molecule by plasmon-enhanced Raman scattering, Nature (London) **498**, 82 (2013).

[44] J. Lee, K. T. Crampton, N. Tallarida, and V. A. Apkarian, Visualizing vibrational normal modes of a single molecule with atomically confined light, Nature (London) **568**, 78 (2019).
[45] J. Xu, X. Zhu, S. Tan, Y. Zhang, B. Li, Y. Tian, H. Shan, X. Cui, A. Zhao, Z. Dong, J. Yang, Y. Luo, B. Wang, and J. G. Hou, Determining structural and chemical heterogeneities of surface species at the single-bond limit, Science **371**, 818 (2021).
[46] Y. Litman, F. P. Bonafé, A. Akkoush, H. Appel, and M. Rossi, First-principles simulations of tip enhanced Raman scattering reveal active role of substrate on high-resolution images, J. Phys. Chem. Lett. **14**, 6850 (2023).
[47] R. Chen and L. Jensen, Interpreting chemical enhancements of surface-enhanced Raman scattering, Chem. Phys. Rev. **4** (2023).
[48] See Supplemental Material at http://link.aps.org/supplemental/10.1103/PhysRevLett.134.206901 for detailed experimental and theoretical methods, additional figures, and tables, which includes Refs. [4,8,9,11,14,15,17,18,40,41,46,49–64].
[49] R. L. Summers, Empirical observations on the sensitivity of hot cathode ionization type vacuum gages, NASA Technical Report NASA-TN-D-5285, 1969.
[50] V. Blum, R. Gehrke, F. Hanke, P. Havu, V. Havu, X. Ren, K. Reuter, and M. Scheffler, *Ab initio* molecular simulations with numeric atom-centered orbitals, Comput. Phys. Commun. **180**, 2175 (2009).
[51] V. Gavini *et al.*, Roadmap on electronic structure codes in the exascale era, Model. Simul. Mater. Sci. Eng. **31**, 063301 (2023).
[52] V. G. Ruiz, W. Liu, E. Zojer, M. Scheffler, and A. Tkatchenko, Density-functional theory with screened van der Waals interactions for the modeling of hybrid inorganic-organic systems, Phys. Rev. Lett. **108**, 146103 (2012).
[53] J. Hermann and A. Tkatchenko, Density functional model for van der Waals interactions: Unifying many-body atomic approaches with nonlocal functionals, Phys. Rev. Lett. **124**, 146401 (2020).
[54] B. Cirera, Y. Litman, C. Lin, A. Akkoush, A. Hammud, M. Wolf, M. Rossi, and T. Kumagai, Charge transfer-mediated dramatic enhancement of Raman scattering upon molecular point contact formation, Nano Lett. **22**, 2170 (2022).
[55] Y. Kunisada and H. Kasai, Hindered rotational physisorption states of H_2 on Ag(111) surfaces, Phys. Chem. Chem. Phys. **17**, 19625 (2015).
[56] V. Kapil *et al.*, i-PI 2.0: A universal force engine for advanced molecular simulations, Comput. Phys. Commun. **236**, 214 (2019).
[57] C. Schwartz, High-accuracy approximation techniques for analytic functions, J. Math. Phys. (N.Y.) **26**, 411 (1985).
[58] D. T. Colbert and W. H. Miller, A novel discrete variable representation for quantum mechanical reactive scattering via the *S*-matrix Kohn method, J. Chem. Phys. **96**, 1982 (1992).
[59] Y. Jiang, S. Pillai, and M. A. Green, Realistic silver optical constants for plasmonics, Sci. Rep. **6**, 30605 (2016).
[60] B. Pettinger, K. F. Domke, D. Zhang, G. Picardi, and R. Schuster, Tip-enhanced Raman scattering: Influence of the tip-surface geometry on optical resonance and enhancement, Surf. Sci. **603**, 1335 (2009).
[61] L. Wolniewicz, The $X\,^1\Sigma_g^+$ state vibration-rotational energies of the H_2, HD, and D_2 molecules, J. Chem. Phys. **78**, 6173 (1983).
[62] D. K. Veirs and G. M. Rosenblatt, Raman line positions in molecular hydrogen: H_2, HD, HT, D_2, DT, and T_2, J. Mol. Spectrosc. **121**, 401 (1987).
[63] G. K. Teal and G. E. MacWood, The Raman spectra of the isotopic molecules H_2, HD, and D_2, J. Chem. Phys. **3**, 760 (1935).
[64] B. N. J. Persson and R. Ryberg, Vibrational line shapes of low-frequency adsorbate modes: CO on Pt(111), Phys. Rev. B **40**, 10273 (1989).
[65] E. W. Smeets and G.-J. Kroes, Designing new SRP density functionals including non-local vdW-DF2 correlation for H_2 + Cu(111) and their transferability to H_2 + Ag(111), Au(111) and Pt(111), Phys. Chem. Chem. Phys. **23**, 7875 (2021).
[66] J. Cui, Y. Zhang, and Z.-C. Dong, Atomistic polarization model for Raman scattering simulations of large metal tips with atomic-scale protrusions at the tip apex, Nanophotonics **12**, 4031 (2023).
[67] R. Kamimura, T. Kondo, K. Motobayashi, and K. Ikeda, Surface-enhanced electronic Raman scattering at various metal surfaces, Phys. Status Solidi B **259**, 2100589 (2022).
[68] T. E. Markland, S. Habershon, and D. E. Manolopoulos, Quantum diffusion of hydrogen and muonium atoms in liquid water and hexagonal ice, J. Chem. Phys. **128**, 194506 (2008).
[69] H. D. Megaw and F. Simon, Density and compressibility of solid hydrogen and deuterium at 4.2 K, Nature (London) **138**, 244 (1936).
[70] Z.-F. Cai, N. Kumar, and R. Zenobi, Probing on-surface chemistry at the nanoscale using tip-enhanced Raman spectroscopy, CCS Chem. **5**, 55 (2023).
[71] J.-L. Yang, Y.-W. Zhou, M.-Y. Jia, Q. Liu, and Z.-F. Cai, Insights into heterogeneous catalysis by tip-enhanced Raman spectroscopy, ChemCatChem **16**, e202400370 (2024).
[72] A. Shiotari, S. Liu, G. Trenins, T. Sugimoto, M. Wolf, M. Rossi, and T. Kumagai, Source Data for Picocavity-Enhanced Raman Spectroscopy of Physisorbed H_2 and D_2 Molecules, https://doi.org/10.5281/zenodo.15412836 (2025).